

A synergistic strategy to develop photostable and bright dyes with long Stokes shift for super-resolution microscopy

gangwei jiang

Hunan University

Tian-Bing Ren

Hunan University <https://orcid.org/0000-0002-5774-8306>

Elisa D'Este

Max-Planck Institute for medical research

mengyi xiong

Hunan University

Bin Xiong

Hunan University <https://orcid.org/0000-0002-1575-5954>

Kai Johnsson

Max Planck Institute for Medical Research <https://orcid.org/0000-0002-8002-1981>

Xiaobing Zhang

Hunan University <https://orcid.org/0000-0002-4010-0028>

Lu wang (✉ lu.wang@mr.mpg.de)

max-planck institute for medical research <https://orcid.org/0000-0001-8412-2985>

Lin Yuan

Hunan University <https://orcid.org/0000-0002-1015-5319>

Article

Keywords: fluorescent probes, fluorophores, quinoxaline motif

Posted Date: September 23rd, 2021

DOI: <https://doi.org/10.21203/rs.3.rs-885436/v1>

License:   This work is licensed under a Creative Commons Attribution 4.0 International License.

[Read Full License](#)

Version of Record: A version of this preprint was published at Nature Communications on April 27th, 2022. See the published version at <https://doi.org/10.1038/s41467-022-29547-3>.

Abstract

The quality and application of super-resolution fluorescence imaging greatly lie in the properties of fluorescent probes. However, conventional fluorophores in a cellular environment often suffer from low brightness, poor photostability, and short Stokes shift (< 30 nm). Here we report a synergistic strategy to simultaneously improve such properties of regular fluorophores. Introduction of quinoxaline motif with fine-tuned electron density to conventional rhodamines generates new dyes with vibronic structure and inhibited twisted-intramolecular-charge-transfer (TICT) formation synchronously, thus increasing the brightness and photostability as well as Stokes shift. The new fluorophore **BDQF-6** exhibits around twofold greater brightness ($\epsilon \times \Phi = 6.6 \times 10^4 \text{ L}\cdot\text{mol}^{-1}\cdot\text{cm}^{-1}$) and Stokes shift (56 nm) than its parental fluorophore, Rhodamine B. Importantly, in Stimulated Emission Depletion (STED) microscopy, **BDQF-6** derived probe possesses a superior photostability and thus renders threefold more frames than carbopyronine- and JF608-based probes, known as photostable fluorophores for STED imaging. More **BDQF-6** derivatives were developed next, allowing us to perform wash-free organelles (mitochondria and lysosome) staining and protein labeling with ultrahigh signal-to-noise ratios (up to 106 folds) in confocal and STED microscopy of live cells, or two-photon and 3D STED microscopy of fixed cells. Furthermore, the strategy was well generalized to different types of dyes (pyronin, rhodol, coumarin, and Boranil), offering a new class of bright and photostable fluorescent probes with long Stokes shift (up to 136 nm) for bioimaging and biosensing.

Introduction

Super-resolution microscopy that breaks the diffraction limit of light offers a powerful tool to investigate cellular biology on a molecular scale^{1,2,3}. The combination of Stimulated Emission Depletion (STED) microscopy and suitable labeling strategies enables the real-time observation of cellular structures and biological processes with high spatial and temporal resolution^{4,5}. However, the high-powered depletion laser beam in STED imaging causes severe photobleaching, resulting in more stringent requirements for fluorescent probes^{6,7}. The ideal fluorescent probe for super-resolution imaging should possess (1) high brightness to enable visualization of low-abundant targets, (2) good photostability to permit long-term tracking and high-fidelity imaging under high-powered STED laser, (3) long Stokes shift to reduce fluorescence self-quenching and increase signal-to-noise ratio and (4) various excitation/emission wavelengths to enable monitoring of multi-targets at the same time^{3,8,9}. In addition, cell permeable dyes are also highly desired in live-cell imaging to avoid the potential interference and artificial errors from the sample fixation or invasive techniques, such as bead loading¹⁰ and microinjection¹¹. However, the development of such probes is particularly challenging and thus the ideal probe has not yet been reported.

Rhodamine and its derivatives are the most popular fluorophores applied in STED microscopy due to their exceptional properties, including high brightness, good photostability, and various excitation/emission wavelengths³. Recently, some practical strategies³ have been reported to further improve their properties,

including brightness^{12, 13, 14, 15, 16, 17}, cell-permeability^{18, 19}, fluorogenicity^{18, 19, 20, 21}, photostability^{15, 17, 22}, and Stokes shift^{23, 24, 25, 26}, to meet the requirements of various fluorescence imaging techniques. In the excited state of regular rhodamines (e. g., Rhodamine B (RhB)) the dialkylamine groups form the twisted-internal-charge-transfer (TICT) state through a C-N bond rotation, which leads to energy relaxation without emission of a photon but with a rapid nonradiative decay (Fig. 1)²⁷. The nonradiative state can also produce radicals after reaction with molecular oxygen and often cause photobleaching, photobleaching, and fluorescence signal blinking^{6, 22, 27, 28} (Supplementary Fig. 1). Thus, inhibition of the TICT effect by reducing or preventing the rotation of the C-N bond in rhodamines (e.g., replacing dialkylamino with 7-azabicyclo[2.2.1]heptane¹⁷, azetidine, or aziridine¹⁵) was utilized to improve brightness and photostability (Fig. 1). Another method is to increase the energy barrier of forming TICT state by reducing electron density in fluorophore scaffold through introducing electron-withdrawing groups (EWGs) (e. g., quaternary piperazine¹⁴ or sulfone-functionalized piperidine moieties¹³) (Fig. 1). Even such methods have greatly improved the brightness of various fluorophores, the severe photobleaching caused by the high-powered depletion laser in STED microscopy still exists and has become a significant bottleneck⁷. In addition, the above modifications in the symmetric structure of rhodamines usually produce a small Stokes shift (20–30 nm) with a large overlap between the excitation and emission spectra, which often causes self-quenching and low signal-to-noise ratio in fluorescence imaging^{29, 30}. The smaller Stokes shift also requires more strict filter settings in the fluorescence microscopy. To address this problem, some strategies have been proposed to modify rhodamines' scaffold. For example, vibronic structure in fluorophores was produced to induce strong internal conversion between HOMO and LUMO of fluorophores, thus significantly increasing Stokes shift²⁴. However, the brightness of these dyes in aqueous solution is usually unsatisfying^{23, 24}. Till now, to the best of our knowledge, no universal strategy was reported to enable the improvement of brightness, photostability and Stokes shift all at once.

To address the above challenges, we combined the strength of different design methods and proposed a synergistic strategy to develop a new type of asymmetric rhodamines (**BDQF**) that combines TICT inhibition and vibronic structure (Fig. 1). Among these rhodamine derivatives, **BDQF-6** with 2-(2,2,2-trifluoroethyl)octahydropyrrolo[1,2-a]pyrazine moiety showed a significantly enhanced brightness, improved photostability, and expanded Stokes shift while preserving good cell permeability. **BDQF-6**-derived probes showed excellent performance in wash-free organelles staining and protein labeling in confocal and STED microscopy. The new design strategy was further extended to other widely-used fluorophores, transferring them to a new class of fluorescent probes and biosensors with great brightness, high photostability, and long Stokes shift.

Results

Rational Design of bright and photostable dyes with long Stokes shift. Recently reported strategies offer two important routes to improve properties of regular rhodamines: symmetric xanthene with inhibition of TICT effect and asymmetric xanthene with vibronic structure (Fig. 1). However, none of the reported approaches can simultaneously improve brightness, photostability, and Stokes shift. Thus, we assumed

that a combination of vibronic structure and TICT inhibition could open up an opportunity to develop a new type of bright and photostable fluorophores with long Stokes shift (Fig. 1).

We started from the asymmetric rhodamine to enlarge the Stokes shift and **BDQF-1** was thus synthesized based on the reported work^{23,24}. Consistent with previous work, **BDQF-1** displays a greatly increased Stokes shift (99 nm) than RhB (27 nm)²³. However, only a weak fluorescence signal was collected from **BDQF-1** in PBS buffer solution (Supplementary Fig. 4 and Supplementary Table 1), limiting its application in a cellular environment. Inspired by the reported approaches that optimize the brightness through tuning the electron density in xanthene^{13, 14, 19}, we thus developed new dyes **BDQF-(2-7)** that contained various EWGs in quinoxaline moiety of the fluorophore scaffold. Such fluorophores can be easily synthesized by the condensation of 2-(4-diethylamino-2-hydroxybenzoyl)benzoic-acid and quinoxaline moieties **BDQ-(1-6)**, which were generated *via* nucleophilic substitution (**BDQ-(2-5)**) or amidation followed by the reduction reaction (**BDQ-6**) (Fig. 2a and Supplementary Scheme 1).

In **BDQF** dyes, the emission maxima (λ_{em}) showed a clear hypochromatic shift from 673 nm to 590 nm as the electron withdrawing ability of quinoxaline substituents increases, which showed a linear correlation between λ_{em} and Hammett substituent constant (σ_p) (Supplementary Fig. 5). The inductive effect of the substituents was further demonstrated by the well-regulated changing of the electron density of xanthene scaffolds in DFT calculation (Supplementary Fig. 6). Meanwhile, we found that the stronger the electron withdrawing ability of quinoxaline in **BDQF-(1-6)** was, the higher brightness and smaller Stokes shift the fluorophores displayed (Fig. 2b). Considering the importance of both brightness and Stokes shift, we identified **BDQF-6** with 2-(2,2,2-trifluoroethyl) octahydropyrrolo[1,2-a]pyrazine group as the best fluorophore. It displayed a 2.4-fold increase in quantum yield (0.74) and 2-fold enhancement in brightness ($\epsilon \times \Phi = 6.6 \times 10^4 \text{ L}\cdot\text{mol}^{-1}\cdot\text{cm}^{-1}$) in aqueous solution compared to its parental fluorophore, RhB. Meanwhile, **BDQF-6** showed a red-shifted excitation/emission spectra of 578 nm/634 nm, generating a long Stokes shift of 56 nm (Fig. 2c). In addition, **BDQF-6** displayed significantly higher photostability and less photobleaching over RhB under the illumination of light at 530 nm for 80 min (Fig. 2d and Supplementary Fig. 7-9). We also observed highly consistent fluorescence intensity and lifetime of **BDQF-6** in various solvents or buffer solutions with abundant proteins, which cannot be achieved in RhB (Fig. 2e, 2f, Supplementary Fig. 10). Importantly, DFT calculation of **BDQF-6** showed the asymmetric electron distribution in the HOMOs (Fig. 2g) and increased energy barrier to form TICT state (Fig. 2h), thus indicating the coincidence of vibronic feature²⁴ and TICT inhibition¹⁴ in **BDQF-6**. The outstanding performance of **BDQF-6** thus demonstrates the exceptional strength of the proposed synergistic strategy in the dye development.

Evolution of BDQF-6 derived probes for live-cell confocal imaging. We next incubated HeLa cells with **BDQF-6** to evaluate its cell permeability, brightness, and photostability in live-cell imaging. **BDQF-6** showed a similarly fast cellular staining as RhB, while possessed a stronger fluorescence signal. The significantly increased fluorescence signal is assumed to be due to the combination of higher brightness

and larger Stokes shift from **BDQF-6** (Supplementary Fig. 11). Importantly, RhB can be easily photobleached within 10 min under continuous irradiation at 560 nm, while negligible signal change of **BDQF-6** was observed, indicating the outstanding photostability of **BDQF-6** in cellular environment (Fig. 3a and Supplementary Fig. 12-13). To achieve the specific labeling of target protein, we next synthesized **BDQF-6** ligand (**BDQF-9-Halo**) from carboxyl-containing **BDQF-6** (**BDQF-9**) for labeling HaloTag, a widespread protein tag³¹ (Fig. 3b). Incubation of live HeLa cells expressing

a HaloTag–histone 2B (H2B) fusion with **BDQF-9-Halo** offered a bright nuclear staining (Supplementary Fig. 14), providing 1.5-fold stronger fluorescence signal than RhB derivatives, RhB-Halo (Fig. 3c-3f). Interestingly, compared to RhB-Halo, **BDQF-9-Halo** displayed a much lower cytoplasmic background, which thus endowed a higher nuclei-to-cytosol signal ratio ($F_{\text{cyt}}/F_{\text{nuc}}=18$) without any washing steps (Fig. 3c-3f). Since it was reported that shifting the equilibrium from the zwitterionic form to the spirocyclic form could help optimize the cell permeability and fluorogenicity^{18,19}, we next transferred the carboxyl group in **BDQF-9** to acyl 2,2,2-trifluoroethylamide, producing probe **BDQF-10**. D_{50} , representing the dielectric constant at which half of the fluorophore population is in the zwitterionic form, has been commonly applied to evaluate the equilibrium between zwitterionic and spirocyclic form³². Based on the reported work, **BDQF-10** with a D_{50} of 45 was thus expected to be a good candidate for generating fluorogenic probes (Supplementary Fig. 15). The subsequently synthesized **BDQF-10-Halo** HaloTag ligand showed a large increase in absorbance (23-fold) and fluorescence intensity (490-fold) upon binding to HaloTag (Supplementary Fig. 16). Consistently, the intracellular background signal of live HeLa cells treated with **BDQF-10-Halo** is extremely low, thereby offering a superior signal-to-noise ratio in nuclear protein labeling ($F_{\text{nuc}}/F_{\text{cyt}} = 106$) (Fig. 3e). Notably, even the formation of spirolactam in **BDQF-10** improves the fluorogenicity and cell permeability (Supplementary Fig. 17), it also reduces the brightness to some extent due to the incomplete recovery to the fluorescent zwitterionic state upon HaloTag binding (Fig. 3f)²¹.

We next extended this bright and photostable fluorophore **BDQF-6** to prepare new probes for organelles staining in living cells. Probe **BDQF-6-Mito** and **BDQF-6-Lyso** were synthesized by one-step esterification and amidation reaction respectively (Supplementary Scheme S1). We succeeded to utilize these probes in fast and high contrast wash-free staining in mitochondria and lysosomes, as confirmed by the colocalization with MitoTracker Green and LysoTracker Green respectively (Fig. 3g-3j and Supplementary Fig. 18-20).

Superior photostability of BDQF-6 derivatives in STED imaging. STED microscopy allows the visualization of biological structures with high spatial and temporal resolution in living cells^{33, 34, 35, 36, 37, 38}. However, the severe photobleaching of fluorophores has greatly limited the frame number collected in STED imaging. Till now, only a very few reported probes for covalently labeling of proteins can provide satisfying performance in STED imaging, especially 3D STED microscopy^{39, 40, 41}. Rhodamine derivatives

(e.g., SiR³², CPY⁴², JF608¹⁵) are the most popular fluorophores in STED imaging due to their good photophysical properties, cell permeability, and photostability³. We thus compared the performance of **BDQF-**, CPY- and JF608-derived probes, which share a similar emission wavelength, in STED microscopy with a 775 nm depletion laser. **BDQF-9-Halo**, CPY-Halo, and JF608-Halo were synthesized and applied for specific staining of vimentin fused with HaloTag in fixed U-2 OS cells. CPY-Halo and JF608-Halo provided STED images with full width at half-maximum (fwhm) resolution of 86±9 and 83±10 nm in the first frame. However, only 2-3 frames of STED images with >50% of the initial fluorescence intensity were obtained due to the rapid photobleaching under a 775 nm depletion laser (Fig. 4a, 4b and Supplementary Fig. 21-22). In contrast, under the identical conditions, **BDQF-9-Halo** offers 9 frames of STED images with >50% of the initial fluorescence intensity while remaining the full width at half-maximum (fwhm) resolution of 57±5 nm (Fig. 4a and 4b and Supplementary Fig. 23-24). When optimizing the imaging settings to obtain the highest resolution, **BDQF-9-Halo** enabled the visualization of vimentin filaments with an fwhm of 37±4 nm (Supplementary Fig. 25). The significantly increased frame numbers and resolution in STED imaging demonstrate the superior photostability of **BDQF-9-Halo**. We thus tried to utilize **BDQF-9-Halo** in 3D STED imaging, which is difficult to be achieved when rapid photobleaching of traditional fluorophores occurs during sequential *xzy*-scan³⁸. Incubation of U-2 OS cells transiently expressing mitochondrial import receptor Tomm20-HaloTag with **BDQF-9-Halo** enabled the construction of 3D STED images of Tomm20 along the whole mitochondria (Fig. 4c and Supplementary Fig. 26). In addition, the excellent cell permeability and high contrast staining utilizing **BDQF-9-Halo** and **BDQF-10-Halo** allowed us to perform the wash-free live-cell STED imaging of vimentin filaments with a resolution of 59±7 nm (Fig. 4d and Supplementary Fig. 27).

Extension of the strategy to different types of fluorophores. Numerous classic fluorophore scaffolds contain the dialkylamino motif and often suffer from TICT, leading to the decreased quantum efficiency and photostability^{14, 15, 47, 48}. Encouraged by the excellent performance of **BDQD-6**, we next extended the strategy to other widely-used fluorophores with different colors. Replacing the dialkylamine with 2-(2,2,2-trifluoroethyl)octahydropyrrolo[1,2-a]pyrazine in the xanthene of rhodol (**BDQD-11**) vastly increased the quantum yield from 0.21 to 0.62 and the brightness from 1.3×10^4 to 3.2×10^4 L·mol⁻¹·cm⁻¹. Meanwhile, **BDQD-11** displayed a red-shifted absorbance/emission maxima from 518 nm/546 nm to 548 nm/612 nm with a long Stokes shift of 64 nm (Table 1 and Supplementary Fig. 28). The confocal imaging of live HeLa cells also indicated the greatly improved photostability of **BDQD-11** than its parental fluorophore (Supplementary Fig. 29). Importantly, similar improvements in the brightness, photostability, and Stokes shift were also found in other xanthene-containing fluorophores, such as pyronin (Table 1 and Supplementary Fig. 28, 30).

We next applied the strategy to coumarin and Boranil that possess very different fluorophore scaffolds. Consistently, the introduction of 2-(2,2,2-trifluoroethyl)octahydropyrrolo[1,2-a]pyrazine motif in **BDQF-(13-15)** also offers dramatically increased brightness (5.1-8.1 folds) and improved photostability

(Supplementary Fig. 31-34 and Supplementary Table 4-5). Notably, **BDQF-15** and **BDQF-14** displayed a large Stokes shift of 136 nm and 92 nm respectively (Table 1). Chloroalkane was next conjugated with **BDQF-16**, an analog of **BDQF-14**, to produce HaloTag ligand **BDQF-16-Halo** (Fig. 5a and Supplementary Scheme 1). Similar to the optical properties of **BDQF-14**, **BDQF-16-Halo** also exhibited a large Stokes shift (110 nm) in aqueous solution (Fig. 5b). Interestingly, probe **BDQF-16-Halo** displayed a good nuclear protein labeling without any washing steps, while its parental probe Coumarin-Halo showed no specific staining under the same conditions (Fig. 5c and 5d). Furthermore, **BDQF-16-Halo** enables the imaging of vimentin filaments in live-cell STED microscopy using a depletion laser of 595 nm (Supplementary Fig. 35). Overall, these results demonstrate that replacing the dialkylamino motif with 2-(2,2,2-trifluoroethyl)octahydropyrrolo[1,2-a]pyrazine is generalizable to different fluorophore scaffolds, producing substantial improvements in brightness, photostability, and Stokes shift simultaneously.

Bright and photostable fluorophores are always highly desired to develop chemical sensors to avoid the false signal from fluorescence photobleaching^{43,44}. It is worth noting that the new strategy only modifies the dialkylamino motif on one side of the xanthene scaffold in Rhodol, which leaves the oxygen atom on the other side free for producing sensors^{45,46}. In proof-of-principle experiments, the phosphate group was conjugated to **BDQF-11** to develop a sensor for qualitatively detecting alkaline phosphatase (ALP) (Fig. 5e). **BDQF-11-ALP** showed ultra-weak fluorescence in buffer solution, while the addition of alkaline phosphatase can remove the phosphate group, thereby resulting in a huge signal enhancement (Fig. 5f and 5g). **BDQF-11-ALP** also displayed good specificity towards ALP in the presence of various biomolecules (Fig. 5h). Hela cells incubated with **BDQF-11-ALP** showed a much stronger fluorescence signal than normal liver L02 cell line (Fig. 5i and Supplementary Fig. 36), probably due to the higher expression level of ALP in tumor cells^{49,50}. Meanwhile, the addition of Na_3VO_4 reduced the ALP level in Hela cells, thus producing a decreased fluorescence signal (Fig. 5i and Supplementary Fig. 36).

Discussion

The chemical structures of fluorophores determine their properties (e.g. brightness, photostability, Stokes shift, wavelength, and cell permeability). However, the reported modification methods can only partially improve such key properties³. Meanwhile, new imaging techniques have a higher requirement for fluorescent probes, such as ultra-high photostability for STED microscopy^{6,51}.

To improve such properties simultaneously, we proposed a new fluorophore scaffold modification method *via* the combination of vibronic structure and TICT inhibition. After systematic modification and testing (Fig. 2), 2-(2,2,2-trifluoroethyl)octahydropyrrolo[1,2-a]pyrazine motif was successfully developed and identified as a unique group to simultaneously improve brightness, photostability, and Stokes shift. The vibronic feature and TICT inhibition from 2-(2,2,2-trifluoroethyl)octahydropyrrolo[1,2-a]pyrazine motif were also confirmed by DFT calculation (Fig. 2g and 2h), supporting the assumption of the synergistic strategy. We thus believe that the increased Stokes shift in **BDQFs** is mainly from the vibronic structure (quinoxaline moiety). At the same time, the enhanced brightness probably results from the inhibition of

TICT formation by decreasing electron density of quinoxaline moiety, which was further confirmed by the significantly lower quantum yields of **BDQF-(17–21)** than **BDQF-(11–16)** (Supplementary Table 2–4). In addition, **BDQF-6** exhibits surprisingly high photostability, which even permits 3-times more frame numbers than CPY and JF608, known as photostable dyes in STED microscopy. The superior photostability of **BDQF-6** is assumed to be the synergetic effect from the vibronic structure and TICT inhibition since both methods were reported to enable the improvement of photostability^{14, 15}. The success of simultaneously improving several properties of classic fluorophores in this work demonstrated the extraordinary strength of the synergistic strategy, which will boost many new design strategies to create the next generation of fluorophores.

RhB is a classic fluorophore that has been utilized to develop numerous fluorescent probes and biosensors^{52, 53}. We first applied this synergistic strategy to transfer RhB to new dye **BDQF-6**, which exhibits around twofold greater in brightness ($\epsilon \times \Phi = 6.6 \times 10^4 \text{ L}\cdot\text{mol}^{-1}\cdot\text{cm}^{-1}$) and Stokes shift (56 nm) (Fig. 2). Importantly, **BDQF-6** displayed exceptional photostability, thus allowing us to perform 3D super-resolution imaging, which is very difficult to be achieved with regular fluorophores (Fig. 3). Notably, **BDQF-6** also showed excellent performance in two-photon microscopy (Supplementary Fig. 37). Since the dialkylamino group is found in most classic fluorophores, this new design strategy can be easily extended to other regular dyes. It is worth noting that the significant improvements were obtained not only in fluorophores containing xanthene scaffold (rhodol, pyronin) but also in the ones with quite distinct scaffolds (coumarin and Boranil) (Table 1). Interestingly, this design strategy is even more effective for coumarin- and Boranil-derived fluorophore **BDQF-14** and **BDQF-15**, which showed around 8-fold increased brightness and dramatically enlarged Stokes shifts of (96–136 nm) in aqueous solution.

This new design strategy utilizes 2-(2,2,2-trifluoroethyl)octahydropyrrolo[1,2-a]pyrazine group to replace the dialkylamino group in fluorophores. Notably, this design strategy only requires structure modification on one side of the xanthene scaffold, thus leaving the other amino or hydroxyl group on the other side free to be functionalized. As a proof of concept, **BDQF-11** was successfully developed for *in vitro* and *in cellulo* ALP sensing. The generality and versatility of the design strategy pave the way to improve many other already existing fluorescent probes and create numerous new ones.

Methods

Detailed synthesis procedures, spectroscopic data of all compounds are provided in the Supplementary Information.

Materials and general methods. Unless otherwise stated, all chemical and biological reagents were purchased from commercial suppliers in analytical grade and used without further purification. All tests are performed at room temperature. ¹H and ¹³C nuclear magnetic resonance (NMR) spectra were recorded on a Bruker DRX-400 spectrometer. Mass spectra were recorded on a Matrix Assisted Laser Desorption Ionization Time of Flight Mass Spectrometry (ultrafleXtreme) or LCQ Advantage ion trap mass spectrometer from Thermo Finnigan or Agilent 1100 HPLC/MS.E.M. spectrometer. UV absorption and

emission spectra were recorded on UV-1800 spectrophotometer (Shimadzu Corporation, Japan) and Hitachi F-4600 spectrofluorometer (Tokyo, Japan) respectively. Confocal microscopy was performed on a Nikon A1 plus confocal microscope. STED microscopy was performed on an Abberior Instruments STED 775/595/RESOLFT Expert Line microscope or an Abberior Instruments STED 775/660/multiphoton Infinity Line microscope.

Confocal live-cell imaging. HeLa cells were incubated with the DMEM containing streptomycin (100 µg/mL), penicillin (100 U/mL) and 10 % FBS at 37°C under 5 wt %/vol CO₂ for 24 h. 5 µL stock solution (1 mM) of **BDQF-(1–21)** was added to 1 mL culture medium (final probe concentration: 5 µM), with which the live HeLa cells were incubated for 30 min before cell imaging. To evaluate ALP levels in different cell lines, live HeLa and L02 cells were cultured in 1 mL phenol-red-free DMEM containing 5 µM **BDQF-11-ALP** for 30 min before imaging. In the control experiment, HeLa cells were firstly cultured with Na₃VO₄ (1 mM) for 1 h, then treated with **BDQF-11-ALP** (5 µL 1 mM stock solutions) and incubated for 30 min before imaging.

To express H2B-Halo in living cells, plasmid LZ10 pbreba-H2B-Halo (#91564, addgene) was transfected into HeLa cells utilizing lipo8000 (Beyotime Biotechnology) following the standard protocols⁵⁴. Live HeLa cells were incubated with 250 nM probe for 0.5–5 h at 37 °C in a 5% CO₂ atmosphere and directly imaged using confocal microscopy without washing steps unless specifically stated. Microscopy conditions: RhB, RhB-Halo, R-3 and **BDQF-(6, 11, 12, 9-Halo, 10-Halo, 12-ALP)**, λ_{ex} 561 nm; detection range 585–675 nm. R-2 and **BDQF-(14, 16-Halo)**, λ_{ex} 488 nm; detection range 500–550 nm. **BDQF-13**, λ_{ex} 405 nm; detection range 500–550 nm. Coumarin-Halo and R 4–6, λ_{ex} 405 nm; detection range 425–475 nm. **BDQF-15**, λ_{ex} 405 nm; detection range 570–620 nm.

The photostability testing in STED microscopy. U-2 OS stably expressing Vimentin-HaloTag cells⁵⁵ were seeded on glass coverslips and incubated in imaging medium that contained 50 nM **BDQF-9-Halo**, CPY-Halo, and JF608 for 6 h at 37 °C. Next, the cells were fixed with 4% PFA for 20 min and quenched for 5 min in NH₄Cl and glycine (both 100 mM), washed in PBS, and mounted in Mowiol. The fixed samples were imaged on an Infinity Line STED microscope equipped with 775 and 660 STED lines, and 518 nm, 561 nm, 640 nm, and multiphoton excitation lines (Abberior Instruments GmbH). Imaging conditions: λ_{ex} 561 nm, detection range 570–700 nm, STED laser 775 nm.

3D STED microscopy. Plasmid pcDNA5-FRT-Tomm20-Halo was transfected into the host cell line U-2 OS using Turbofect (ThermoFisher) following the manufacturer's protocol. U-2 OS cells transiently expressing Tomm20-HaloTag were next incubated in imaging medium that contained 50 nM **BDQF-9-Halo** overnight at 37 °C. The cells were fixed with 4% PFA for 20 min and then quenched for 5 min in NH₄Cl and glycine (100 mM), washed in PBS, and mounted in Mowiol. Imaging was performed on an Expert line STED/RESOLFT system equipped with 595 nm and 775 nm STED lines, and 355 nm, 405 nm, 485 nm, 561 nm, and 775 nm excitation lines (Abberior Instruments). The STED images of mitochondria were collected along the z-axis with a step of 35 nm. The 3D images were constructed in ImageJ with plugin z-

stack depth colorcode. Imaging conditions: λ_{ex} 561 nm, detection range 570–700 nm, STED laser 775 nm.

Live-cell STED microscopy. U-2 OS stably expressing Vimentin-HaloTag cells seeded on glass coverslips were incubated in phenol red-free imaging medium that contained 50 nM **BDQF-9-Halo** or **BDQF-10-Halo** overnight at 37 °C and then imaged without washing with the 775 nm STED line on the Abberior Instruments Infinity Line microscope. For **BDQF-16-Halo**, live U-2 OS stably expressing Vimentin-HaloTag cells were treated with 500 nM probe for 90 min and washed with imaging medium. The STED imaging was collected on the Abberior Expert Line system with excitation wavelength at 485 nm and STED lines at 595 nm. Imaging conditions: **BDQF-9-Halo** and **BDQF-10-Halo**, λ_{ex} 561 nm, detection range 585–675 nm, STED laser 775 nm. **BDQF-16-Halo**, λ_{ex} 485 nm, detection range 505–550 nm, STED laser 595 nm.

References

1. Legant W. R., *et al.* High-density three-dimensional localization microscopy across large volumes. *Nat. Methods* **13**, 359–365 (2016).
2. Liu Z., Lavis L. D., Betzig E. Imaging live-cell dynamics and structure at the single-molecule level. *Mol. Cell* **58**, 644–659 (2015).
3. Wang L., Frei M. S., Salim A., Johnsson K. Small-molecule fluorescent probes for live-cell super-resolution microscopy. *J. Am. Chem. Soc.* **141**, 2770–2781 (2018).
4. Sahl S. J., Hell S. W., Jakobs S. Fluorescence nanoscopy in cell biology. *Nat. Rev. Mol. Cell Biol.* **18**, 685–701 (2017).
5. Blom H., Widengren J. Stimulated emission depletion microscopy. *Chem. Rev.* **117**, 7377–7427 (2017).
6. Zheng Q., Lavis L. D. Development of photostable fluorophores for molecular imaging. *Curr. Opin. Chem. Biol.* **39**, 32–38 (2017).
7. Li D., Qin W., Xu B., Qian J., Tang B. Z. AIE nanoparticles with high stimulated emission depletion efficiency and photobleaching resistance for long-term super-resolution bioimaging. *Adv. Mater.* **29**, 1703643 (2017).
8. Sednev M. V., Belov V. N., Hell S. W. Fluorescent dyes with large Stokes shifts for super-resolution optical microscopy of biological objects: a review. *Methods Appl. Fluoresc.* **3**, 042004 (2015).
9. Sidenstein S. C., D'Este E., Bohm M. J., Danzl J. G., Belov V. N., Hell S. W. Multicolour multilevel STED nanoscopy of actin/spectrin organization at synapses. *Sci. Rep.* **6**, 26725 (2016).
10. McNeil P. L., Warder E. Glass-beads load macromolecules into living cells. *J. Cell Sci.* **88**, 669–678 (1987).
11. Brennan L. D., *et al.* Small molecule injection into single cell *C. elegans* embryos via carbon reinforced nanopipettes. *PLoS ONE* **8**, e75712 (2013).

12. Liu X., *et al.* Aziridinyl fluorophores demonstrate bright fluorescence and superior photostability by effectively inhibiting twisted intramolecular charge transfer. *J. Am. Chem. Soc.* **138**, 6960–6963 (2016).
13. Lv X., Gao C., Han T., Shi H., Guo W. Improving the quantum yields of fluorophores by inhibiting twisted intramolecular charge transfer using electron-withdrawing group-functionalized piperidine auxochromes. *Chem. Commun.* **56**, 715–718 (2020).
14. Ye Z., *et al.* Quaternary piperazine-substituted rhodamines with enhanced brightness for super-resolution imaging. *J. Am. Chem. Soc.* **141**, 14491–14495 (2019).
15. Grimm J. B., *et al.* A general method to improve fluorophores for live-cell and single-molecule microscopy. *Nat. Methods* **12**, 244–250 (2015).
16. Butkevich A. N., *et al.* Fluorescent rhodamines and fluorogenic carbopyronines for super-resolution STED microscopy in living cells. *Angew. Chem. Int. Ed.* **55**, 3290–3294 (2016).
17. Song X., Johnson A., Foley J. 7-azabicyclo[2.2.1]heptane as a unique and effective dialkylamino auxochrome moiety: demonstration in a fluorescent rhodamine dye. *J. Am. Chem. Soc.* **130**, 17652–17653 (2008).
18. Wang L., *et al.* A general strategy to develop cell permeable and fluorogenic probes for multicolour nanoscopy. *Nat. Chem.* **12**, 165–172 (2020).
19. Grimm J. B., *et al.* A general method to fine-tune fluorophores for live-cell and in vivo imaging. *Nat. Methods* **14**, 987–994 (2017).
20. Wang L., Hiblot J., Popp C., Xue L., Johnsson K. Environmentally sensitive color shifting fluorophores for bioimaging. *Angew. Chem. Int. Ed.* **59**, 21880–21884 (2020).
21. Lardon N., *et al.* Systematic tuning of rhodamine spirocyclization for super-resolution microscopy. (2021). DOI: 10.1021/jacs.1c05004.
22. Butkevich A. N., Bossi M. L., Lukinavicius G., Hell S. W. Triarylmethane fluorophores resistant to oxidative photobleaching. *J. Am. Chem. Soc.* **141**, 981–989 (2019).
23. Chen W., Xu S., Day J. J., Wang D., Xian M. A general strategy for development of near-infrared fluorescent probes for bioimaging. *Angew. Chem. Int. Ed.* **56**, 16611–16615 (2017).
24. Ren T. B., *et al.* A general method to increase Stokes shift by introducing alternating vibronic structures. *J. Am. Chem. Soc.* **140**, 7716–7722 (2018).
25. Butkevich A. N., Lukinavicius G., D'Este E., Hell S. W. Cell-permeant large Stokes shift dyes for transfection-free multicolor nanoscopy. *J. Am. Chem. Soc.* **139**, 12378–12381 (2017).
26. Horvath P., Sebej P., Solomek T., Klan P. Small-molecule fluorophores with large Stokes shifts: 9-iminopyronin analogues as clickable tags. *J. Org. Chem.* **80**, 1299–1311 (2015).
27. Grabowski Z. R., Rotkiewicz K., Retting W. Structural changes accompanying intramolecular electron transfer: focus on twisted intramolecular charge transfer states and structures. *Chem. Rev.* **103**, 3899–4031 (2003).

28. Vogel M., Retting W., Sens R., Drexhage K. H. Structural relaxation of rhodamine dyes with different N-substitution patterns: a study of fluorescence decay times and quantum yields. *Chem. Phys. Lett.* **147**, 452–460 (1988).
29. Lavis L. D., Raines R. T. Bright building blocks for chemical biology. *ACS Chem. Biol.* **9**, 855–866 (2014).
30. Peng X., *et al.* Heptamethine cyanine dyes with a large stokes shift and strong fluorescence: a paradigm for excited-state intramolecular charge transfer. *J. Am. Chem. Soc.* **127**, 4170–4171 (2005).
31. Los G. V., *et al.* HaloTag: a novel protein labeling technology for cell imaging and protein analysis. *ACS Chem. Biol.* **3**, 373–382 (2008).
32. Lukinavicius G., *et al.* A near-infrared fluorophore for live-cell super-resolution microscopy of cellular proteins. *Nat. Chem.* **5**, 132–139 (2013).
33. Lukinavicius G., *et al.* Fluorogenic probes for live-cell imaging of the cytoskeleton. *Nat. Methods* **11**, 731–734 (2014).
34. Lukinavicius G., *et al.* Fluorogenic probes for multicolor imaging in living cells. *J. Am. Chem. Soc.* **138**, 9365–9372 (2016).
35. Zheng Q., *et al.* Rational design of fluorogenic and spontaneously blinking labels for super-resolution imaging. *ACS. Cent. Sci.* **5**, 1602–1613 (2019).
36. Butkevich A. N., *et al.* Two-color 810 nm STED nanoscopy of living cells with endogenous SNAP-tagged fusion proteins. *ACS Chem. Biol.* **13**, 475–480 (2018).
37. Spahn C., Hurter F., Glaesmann M., Karathanasis C., Lampe M., Heilemann M. Protein-specific, multicolor and 3D STED imaging in cells with DNA-labeled antibodies. *Angew. Chem. Int. Ed.* **58**, 18835–18838 (2019).
38. Spahn C., Grimm J. B., Lavis L. D., Lampe M., Heilemann M. Whole-cell, 3D, and multicolor STED imaging with exchangeable fluorophores. *Nano Lett.* **19**, 500–505 (2019).
39. Wang C., *et al.* A photostable fluorescent marker for the superresolution live imaging of the dynamic structure of the mitochondrial cristae. *Proc. Natl. Acad. Sci. U S A* **116**, 15817–15822 (2019).
40. Wang C., Taki M., Sato Y., Fukazawa A., Higashiyama T., Yamaguchi S. Super-photostable phosphole-based dye for multiple-acquisition stimulated emission depletion imaging. *J. Am. Chem. Soc.* **139**, 10374–10381 (2017).
41. Yang X., *et al.* Mitochondrial dynamics quantitatively revealed by STED nanoscopy with an enhanced squaraine variant probe. *Nat. Commun.* **11**, 3699 (2020).
42. Grimm J. B., *et al.* Carbofluoresceins and carborhodamines as scaffolds for high-contrast fluorogenic probes. *ACS chem. Biol.* **8**, 1303–1310 (2013).
43. Grzybowski M., *et al.* A highly photostable near-infrared labeling agent based on a phosphorhodamine for long-term and deep imaging. *Angew. Chem. Int. Ed.* **57**, 10137–10141 (2018).

44. Altmen R. B., *et al.* Cyanine fluorophore derivatives with enhanced photostability. *Nat. Methods* **9**, 68–71 (2012).
45. Kamiya M., *et al.* Beta-galactosidase fluorescence probe with improved cellular accumulation based on a spirocyclized rhodol scaffold. *J. Am. Chem. Soc.* **133**, 12960–12963 (2011).
46. Doura T., *et al.* Detection of lacZ-positive cells in living tissue with single-cell resolution. *Angew. Chem. Int. Ed.* **55**, 9620–9624 (2016).
47. Peng T., Yang D. Construction of a library of rhodol fluorophores for developing new fluorescent probes. *Org. Lett.* **12**, 496–499 (2010).
48. Zhang X., Zhang J., Lu X. The fluorescence properties of three rhodamine dye analogues: acridine red, pyronin Y and pyronin B. *J. Fluoresc.* **25**, 1151–1158 (2015).
49. Singh H., Tiwari K., Tiwari R., Pramanik S. K., Das A. Small molecule as fluorescent probes for monitoring intracellular enzymatic transformations. *Chem. Rev.* **119**, 11718–11760 (2019).
50. Zhang J., Chai X., He X. P., Kim H. J., Yoon J., Tian H. Fluorogenic probes for disease-relevant enzymes. *Chem. Soc. Rev.* **48**, 683–722 (2019).
51. Yang Z., *et al.* Super-resolution fluorescent materials: an insight into design and bioimaging applications. *Chem. Soc. Rev.* **45**, 4651–4667 (2016).
52. Hyman L. M., Franz K. J. Probing oxidative stress: Small molecule fluorescent sensors of metal ions, reactive oxygen species, and thiols. *Coord. Chem. Rev.* **256**, 2333–2356 (2012).
53. Wang X. D., Wolfbeis O. S., Meier R. J. Luminescent probes and sensors for temperature. *Chem. Soc. Rev.* **42**, 7834–7869 (2013).
54. Malecki M. J., *et al.* Leukemia-associated mutations within the NOTCH1 heterodimerization domain fall into at least two distinct mechanistic classes. *Mol. Cell. Biol.* **26**, 4642–4651 (2006).
55. Ratz M., Testa I., Hell S. W., Jakobs S. CRISPR/cas9-mediated endogenous protein tagging for RESOLFT super-resolution microscopy of living human cells. *Sci. Rep.* **5**, 9592 (2015).

Declarations

Acknowledgements

This work was supported by the National Natural Science Foundation of China (Project: 21877029 and 22074036 to L. Y., 22004033 to T.R.) and start-up fund from Fudan University (to L.W.). We thank Jasmine Hubrich for the support with cell culture.

Author contributions

L.Y., L.W. and T.R. conceived and designed the project. L.Y., T.R., K.J., and X.Z. supervised and supported the project. G.J. performed the probe syntheses and spectral experiments. G.J., M. X., and B.X. performed confocal imaging experiments. E. D. conducted the STED imaging experiment. The manuscript was

written by G.J., L.W., L.Y., and T.R. and edited by all the coauthors. All authors discussed the results and commented on the manuscript.

Tables

Table 1. Spectroscopic data of **BDQF-(11-15)** and reference fluorophores R-(2-6).

Core	Substituent(R)	Name	$\lambda_{ab}(nm)$	$\lambda_{em}(nm)$	Stokes shift/nm	ϕ	$\epsilon(M^{-1}cm^{-1})$	$\epsilon \times \phi / M^{-1}cm^{-1}$	$\Delta(\epsilon \times \phi)$	
	^a	BDQ	BDQF-11	548	612	64	0.62	51000	31620	2.5
		NEt ₂	R-2	518	546	29	0.21	60000	12600	1
	^a	BDQ	BDQF-12	577	623	46	0.71	83300	59140	3.2
		NEt ₂	R-3	552	581	24	0.18	103000	18540	1
	^a	BDQ	BDQF-13	406	513	117	0.55	32400	17820	5.2
		NMe ₂	R-4	372	470	98	0.19	18000	3420	1
	^b	BDQ	BDQF-14	464	556	92	0.67	26200	17550	8.1
		NEt ₂	R-5	430	484	54	0.06	32200	2170	1
	^b	BDQ	BDQF-15	439	575	136	0.40	25100	10000	8.0
		NEt ₂	R-6	401	462	61	0.04	31300	1250	1

^a Measured in PBS (25 mM, pH 7.4); ^b Measured in PBS (25 mM, pH 7.4) containing 20% EtOH. BDQ represents the 2-(2,2,2-trifluoroethyl)octahydropyrrolo[1,2-a]pyrazine moiety. $\Delta(\epsilon \times \phi)$ represents the the ratio of the increased brightness.

Figures

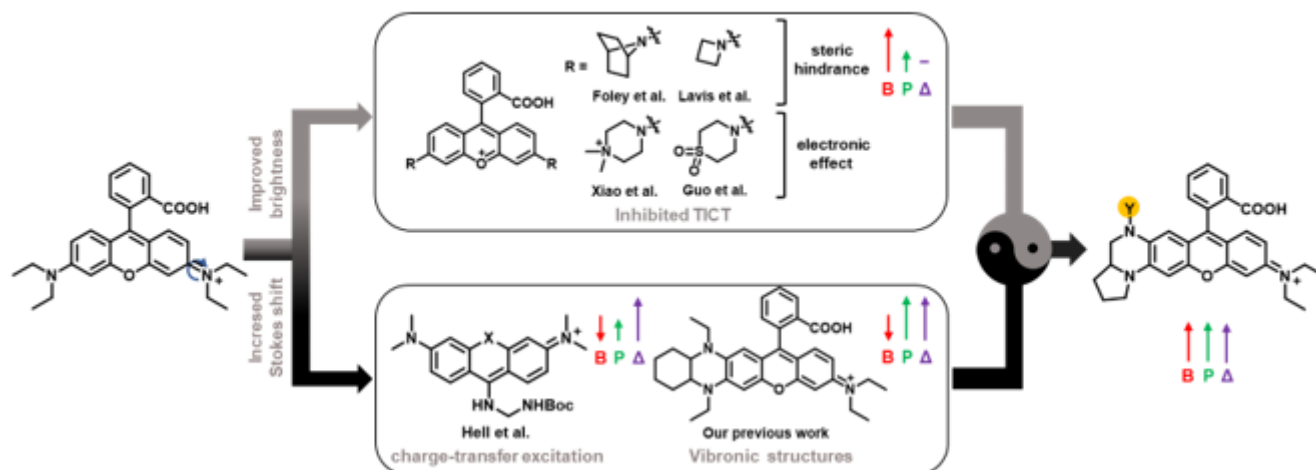
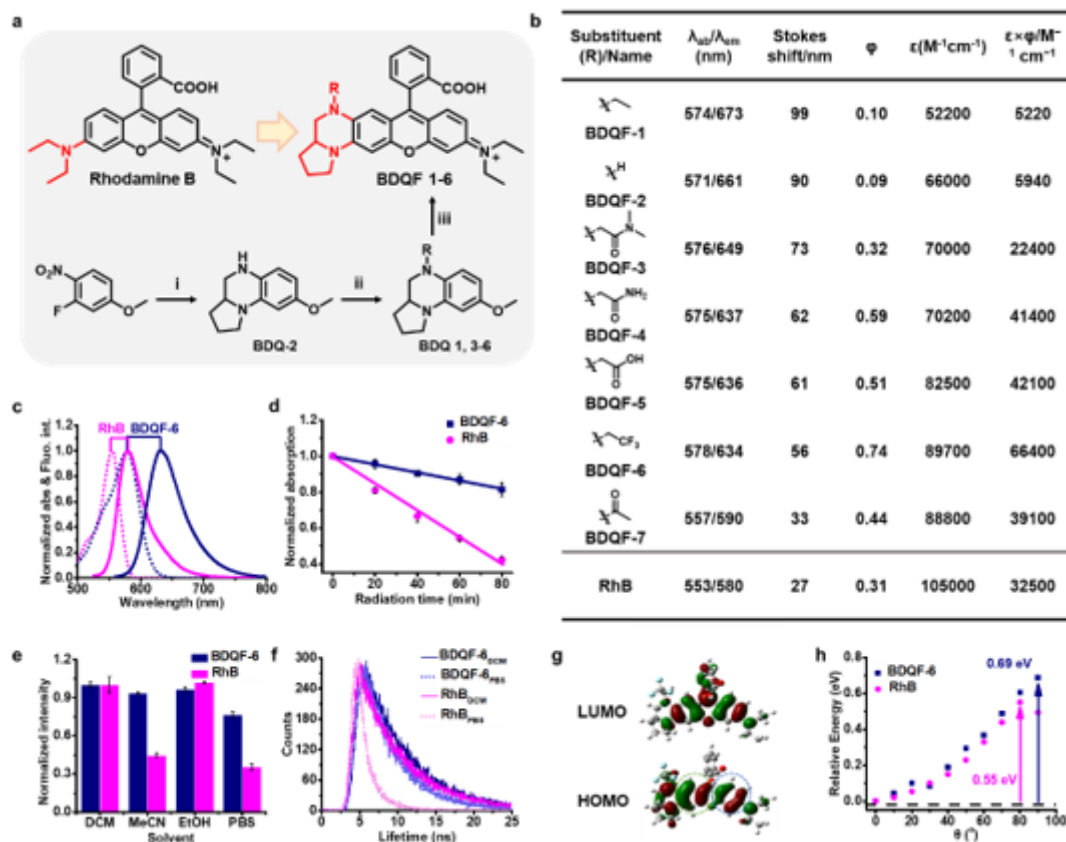


Figure 1

The conventional and new strategies to improve the brightness, photostability, and Stokes shift. In the previous work, brightness, photostability, and Stokes shift can be partially enhanced through inhibiting TICT, generating vibronic structures, or inducing charge-transfer excitation. A new strategy that unites the strength of TCIT inhibition and vibronic structure is proposed to simultaneously increase the brightness, photostability, and Stokes shift. Y (orange circle) denotes the positions used to introduce EWGs to tune electron density. B, P, and Δ represent brightness, photostability, and Stokes shift respectively.

**Figure 2**

Development of BDQF dyes. (a) Synthesis of BDQF dyes. Reaction conditions: i) Proline methyl ester hydrochloride, triethylamine, acetonitrile, reflux, 12 h; methanol, zinc powder, 32% HCl, r.t., 30 min; tetrahydrofuran, NaBH₄, boron trifluoride-diethyl etherate, reflux, 1 h; ii) For BDQ-(2-5), bromide, K₂CO₃, acetonitrile, 90°C, 2 h; for BDQ-6, trifluoroacetic anhydride, tetrahydrofuran, room temperature, 10 min; sodium borohydride, boron trifluoride etherate, reflux, 1 h; iii) 2-(4-Diethylamino-2-hydroxybenzoyl)benzoic acid, methanesulfonic acid, 90°C, 2 h. (b) The photophysical properties of BDQF-(1-7) in aqueous solution. λ_{abs} , absorption maxima; λ_{em} , emission maxima; φ , quantum yield; $\epsilon \times \varphi$, brightness. (c) Normalized absorption and emission spectra of BDQF-6 and RhB. (d) Absorption maxima of BDQF-6 and RhB were plotted as a function of irradiation time with a laser (1 W) at 530 nm. Solution concentrations were adjusted to be comparable to one another in terms of optical density at 530 nm. Error bars, \pm s.e.m. n = 3. (e) Normalized fluorescence maxima intensities of BDQF-6 and RhB in

various solvents. Error bars, \pm s.e.m. $n = 3$. (f) Fluorescence lifetime of BDQF-6 and RhB in DCM and PBS. (g) DFT optimized HOMO and LUMO orbital plots of BDQF-6. (h) Calculated potential energy surfaces of BDQF-6 and RhB in water.

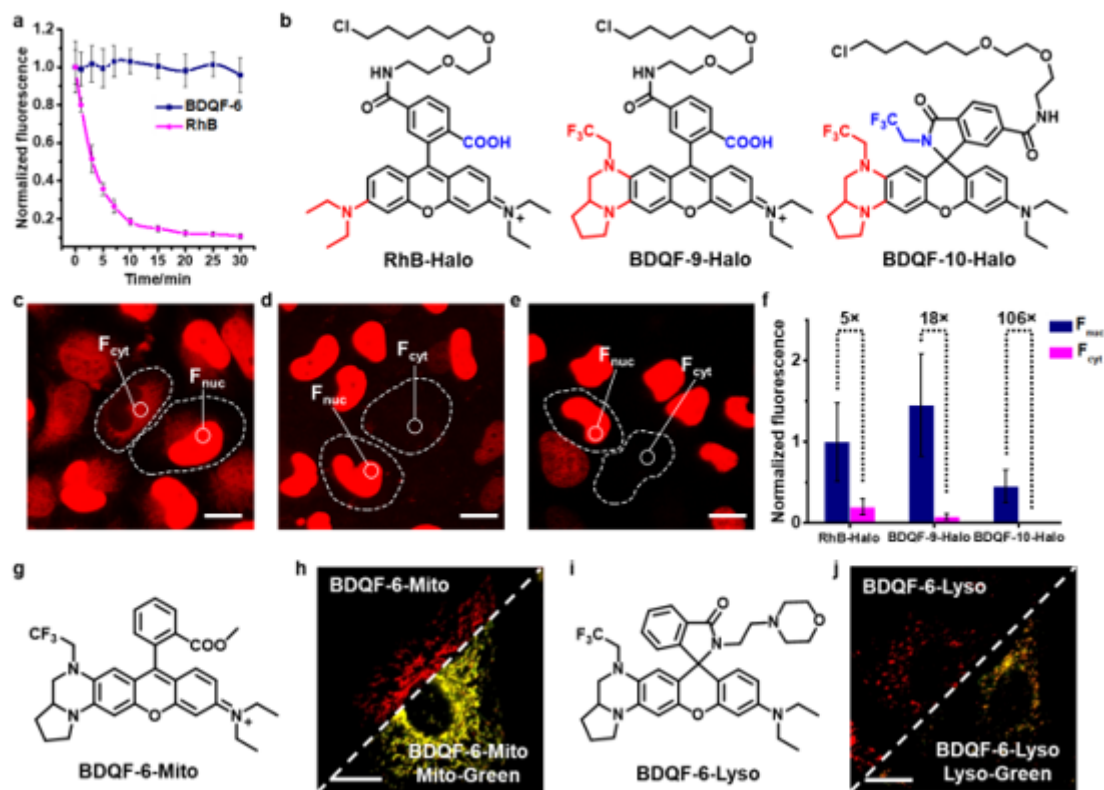


Figure 3

Utility of BDQF derivatives in live-cell imaging. (a) Comparison of the photostability of 5 μ M BDQF-6 or RhB in live HeLa cells with continuous irradiation at 560 nm in confocal microscopy. (b) Structures of HaloTag ligands RhB-Halo, BDQF-9-Halo, and BDQF-10-Halo. (c, d, e) Live-cell, no-wash confocal images (60 \times) of co-cultured H2B-HaloTag-expressing HeLa cells and wild-type HeLa cells with 250 nM RhB-Halo (c), BDQF-9-Halo (d), and BDQF-10-Halo (e), the dashed lines represent the cellular boundary. (f) Fluorescence ratio (F_{nuc}/F_{cyt}) of RhB-Halo, BDQF-9-Halo, and BDQF-10-Halo in live-cell confocal microscopy. Bar plot representing the normalized nuclear signal (F_{nuc} , H2B-Halo-expressed HeLa cells) and the cytosolic signal (F_{cyt} , wild-type HeLa cells). Fluorescence intensities were normalized to the nuclear signal of RhB-Halo. (g) Structure of BDQF-6-Mito. (h) Live-cell, no-wash confocal images of co-incubated HeLa cells with BDQF-6-Mito and Mito-Green. (i) Structure of BDQF-6-Lyso. (j) Live-cell, no-wash confocal images of co-incubated HeLa cells with BDQF-6-Lyso and Lyso-Green. Scale bar, 20 μ m.

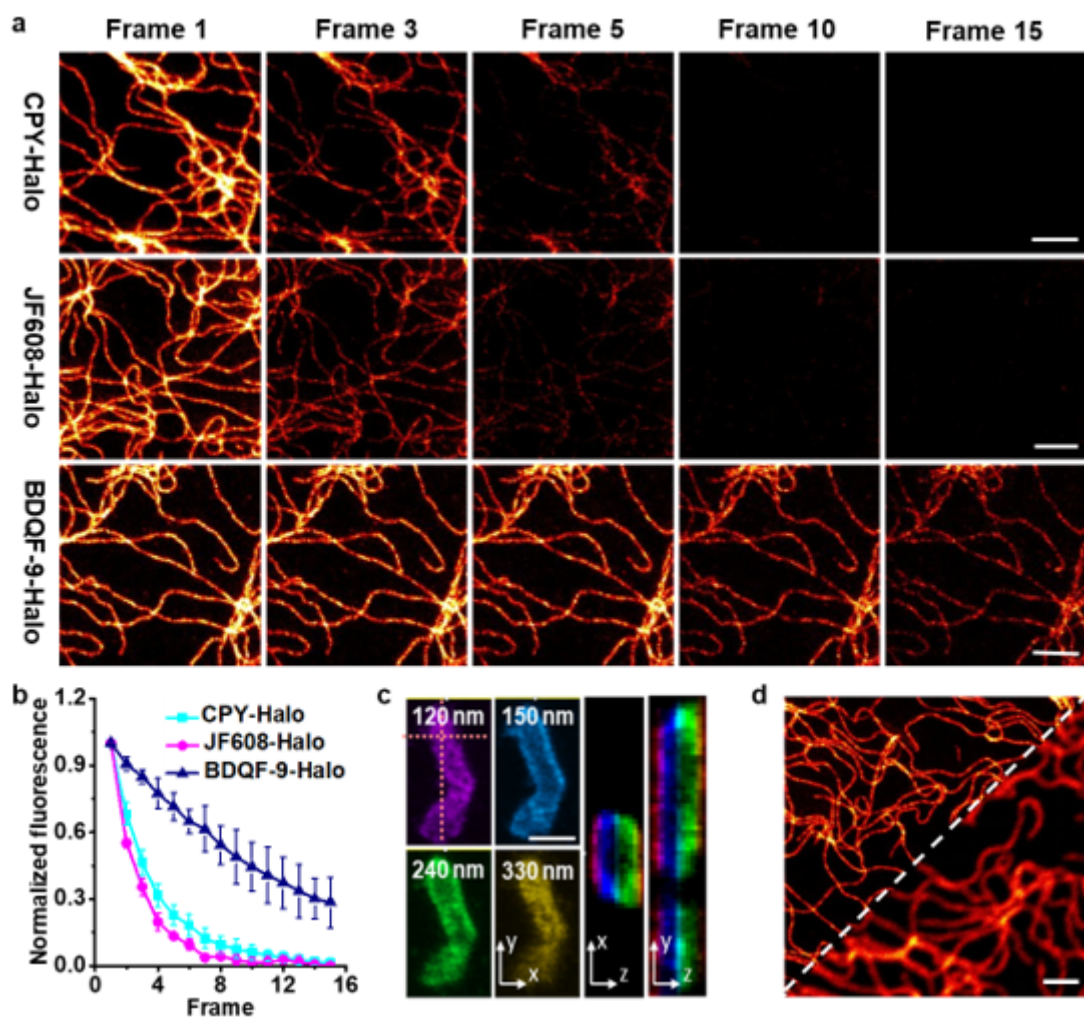


Figure 4

Super-photostable BDQF-9-Halo in 3D and live-cell STED microscopy. (a) Multiframe STED imaging of fixed U-2 OS vimentin-HaloTag-expressing cells labeled with 50 nM CPY-Halo, JF608-Halo, and BDQF-9-Halo respectively (STED at 775 nm). (b) Normalized fluorescence intensities of vimentin filaments labeled with CPY-Halo, JF608-Halo, and BDQF-9-Halo plotted as a function of frame numbers in STED images. (c) 3D STED images of mitochondria in U-2 OS cells expressing Tomm20-Halo labeled with 50 nM BDQF-9-Halo. The images were recorded in sequential xzy-scanning mode. STED images recorded along the z-axis with a step of 35 nm were shown in different colors. Dashed lines indicate the position of XZ and YZ cross sections shown in the right image panel. (d) Wash-free STED images of vimentin filaments in live U-2 OS vimentin-HaloTag-expressing cells labeled with 50 nM BDQF-9-Halo. Scale bar, 1 μ m.

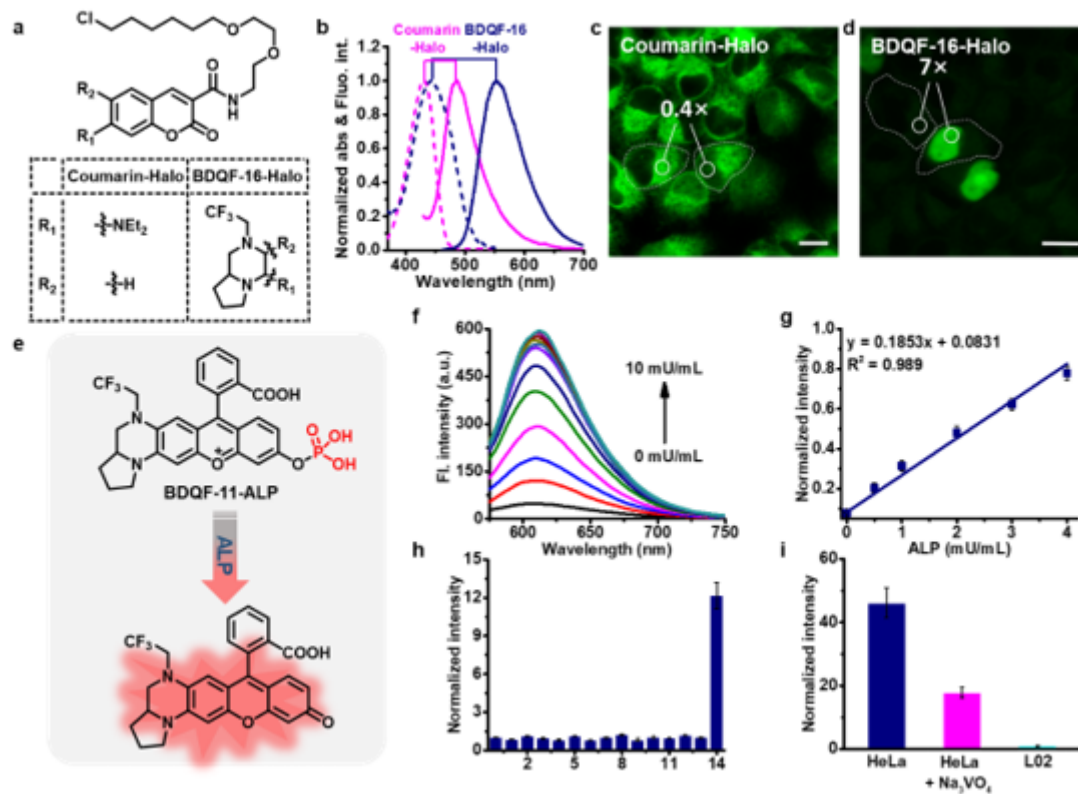


Figure 5

Application of BDQF derivatives in bioimaging and biosensing. (a) Structures of BDQF-16-Halo and Coumarin-Halo. (b) Normalized absorption and emission spectra of BDQF-16-Halo and Coumarin-Halo. (c, d) No-wash live-cell confocal images of co-cultured normal HeLa cells and HeLa cells expressing H2B-Halo labeled with 250 nM Coumarin-Halo (c) or BDQF-16-Halo (d). Scar bar, 20 μ m. (e) Structure of BDQF-11-ALP and its sensing mechanism. (f) The fluorescence spectra of BDQF-11-ALP upon addition of ALP (0-10 mU/mL) in 10 mM tris-HCl buffer (pH 7.4). λ_{exc} = 560 nm. (g) Linear fitting curve of BDQF-11-ALP at 615 nm against ALP from 0 to 4 mU/mL. Error bars, \pm s.e.m. n = 3. (h) Normalized fluorescence responses of BDQF-11-ALP (5 μ M) to various biomolecules: (0) probe alone (5 μ M); (1) Na⁺ (100 μ M); (2) K⁺ (100 μ M); (3) Cysteine (100 μ M); (4) Homocysteine (100 μ M); (5) GSH (1 mM); (6) H₂S (100 μ M); (7) H₂O₂ (100 μ M); (8) ONOO⁻ (5 μ M); (9) HClO (5 μ M); (10) Butyrylcholinesterase (BchE, 10 mU/mL); (11) Acetylcholinesterase (AChE, 10 mU/mL); (12) Esterase (10 mU/mL); (13) Nitroreductase (NTR, 400 mU/mL); (14) Alkaline phosphatase (ALP, 5 mU/mL). Error bars, \pm s.e.m. n = 3. (i) Evaluation of BDQF-11-ALP in sensing ALP of live L02 cells and Hela cells. Live L02 cells and Hela Cells were incubated with BDQF-11-ALP for 30 min, or pre-incubated with 200 μ M Na₃VO₄ for 1 h prior to imaging.

Supplementary Files

This is a list of supplementary files associated with this preprint. Click to download.

- [GangweietaISupportinginformation.docx](#)